Article

Direct Microscopy Imaging of Nonuniform Carrier Transport in Polycrystalline Cadmium Telluride

Chuanxiao Xiao, Chun-Sheng Jiang, Kevin Blaine, ..., Mowafak M. Al-Jassim, Nancy M. Haegel, Helio Moutinho

chuanxiao.xiao@nrel.gov

HIGHLIGHTS

Inhomogeneous local carrier transport is critical in polycrystalline semiconductors

Visualize local charge transport inside single grains and across grain boundaries

Coexistence of carrier drift, diffusion, and recombination in polycrystalline CdTe

Inhomogeneous local carrier transport is critical in polycrystalline semiconductor applications. Xiao et al. resolve the coexistence with microscopic transport imaging and other physical arguments. The results provide visualization of local charge transport inside individual grains and across grain boundaries, which is critical to understanding and engineering polycrystalline solar technology.

Article

Direct Microscopy Imaging of Nonuniform Carrier Transport in Polycrystalline Cadmium Telluride

Chuanxiao Xiao,[1,3,*] Chun-Sheng Jiang,[1] Kevin Blaine,[2] Mahisha Amarasinghe,[1] Eric Colegrove,[1] Wyatt K. Metzger,[1] Mowafak M. Al-Jassim,[1] Nancy M. Haegel,[1] and Helio Moutinho[1]

SUMMARY

Inhomogeneous microscopic carrier transport is difficult to study, but important in many condensed-matter applications. For example, the role of grain boundaries (GBs) in polycrystalline semiconductors has been controversial for 20 years. In cadmium telluride (CdTe) solar cells, electron-beam-induced current (EBIC) measurements consistently demonstrate enhanced current collection along GBs, which is argued as evidence for interpenetrating CdTe *p-n* current-collection networks critical to high efficiency. Conversely, cathodoluminescence (CL) measurements consistently indicate that GBs are deleterious low-lifetime regions. Here, we apply transport imaging (TI) in conjunction with spatially correlated EBIC, CL, and scanning Kelvin probe force microscopy measurements to understand carrier drift, diffusion, and recombination in polycrystalline CdTe. We simultaneously observe GB potential wells, reduced carrier lifetime at GBs, and seemingly contradictory enhanced GB current collection, and then describe their coexistence with microscopic TI and physical arguments. The results provide visualization of inhomogeneous transport that is critical to understanding and engineering polycrystalline solar technology.

INTRODUCTION

Carrier transport and diffusion are often assumed to be homogeneous, but there are many instances in condensed-matter systems in which this is not the case. This is particularly true for polycrystalline semiconductors, where grain boundaries (GBs) and other interfaces interrupt the lattice periodicity. The effects on different semiconductor applications such as photovoltaics have been difficult to determine generally, and consequently, they have often been overlooked or are controversial. For example, cadmium telluride (CdTe) photovoltaics is the market-leading thin-film solar conversion technology. In recent years, the cell efficiency has advanced greatly from 16.7% to 22.1%,[1,2] mainly due to increased short-circuit current density, along with advances in open-circuit voltage (V_{oc}) and fill factor. Many innovations have been developed, such as removing the CdS window layer,[3,4] incorporating a $CdSe_xTe_{1-x}$ alloy into the CdTe absorber,[5–7] *in situ* group V doping,[8,9] defect engineering by switching from Te-rich to Cd-rich stoichiometry,[10,11] and ohmic back-contact engineering of ZnTe-based materials.[12,13] However, despite the commercial maturity of this technology, the carrier transport throughout the material in different directions has been difficult to study, creating poor understanding and controversy.

A $CdCl_2$ anneal has been essential to fabricate high-efficiency polycrystalline CdTe solar cells. Experiments have indicated that the anneal enhances grain growth and

[1]National Renewable Energy Laboratory, Golden, CO 80401, USA

[2]Air Force Institute of Technology, Wright-Patterson AFB, OH 45433, USA

[3]Lead Contact

*Correspondence: chuanxiao.xiao@nrel.gov

https://doi.org/10.1016/j.xcrp.2020.100230

recrystallization, intermixes CdS or CdSeTe and CdTe for junction improvement, and passivates bulk defects.[14–18] In addition, multiple characterization techniques—such as cathodoluminescence (CL),[19,20] time-of-flight secondary-ion mass spectrometry,[21,22] scanning microwave impedance microscopy,[23,24] and scanning transmission electron microscopy[25,26]—as well as first-principles theory calculations[27,28] indicate that Cl segregates to and passivates the GBs after $CdCl_2$ treatment. However, the GB passivation is not perfect, and CL studies consistently indicate that nearly all of the GB regions have lower lifetimes relative to the grain interior (GI) after $CdCl_2$ treatment.[19,20] In contrast, independent electron-beam (e-beam)-induced current (EBIC) measurements reveal enhanced photocurrents at GBs.[29–34] This observation has been used to argue that GBs form three-dimensional *p-n* networks, which increase photocurrent collection and describe why polycrystalline solar cells outperform single-crystal devices.[32–34] However, there has been significantly more work on polycrystalline device optimization than on single crystals, and the latter have produced higher V_{oc}.[8,35–37] Consequently, there is debate about the role of GBs in polycrystalline CdTe solar cells and the ability of EBIC measurements to determine their electrical properties.[38,39]

Here, we study nonuniform carrier transport in CdTe intra- and intergrains before and after $CdCl_2$ annealing by performing spatially correlated EBIC, near-field CL (NFCL), scanning Kelvin probe force microscopy (KPFM), and NF transport imaging (TI). The latter can image inhomogeneous transport at different locations and along different directions by direct visualization with resolution that can exceed the diffraction limit,[40,41] illustrating the combined effect of carrier diffusion, drift, and recombination as a result of localized carrier generation.

RESULTS AND DISCUSSION

The samples were made by depositing CdTe on glass/SnO_2-bilayer/MgZnO substrates before and after $CdCl_2$ anneals (see Experimental Procedures). EBIC maps the collection of electric currents by e-beam local generation of minority carriers.[42] The EBIC image represents the collected current at every pixel as the e-beam is scanned over the sample surface. The minority carriers generated by the e-beam diffuse and drift across the device, and those that reach the depletion region and are collected contribute to the EBIC signal. Figure 1 illustrates that the $CdCl_2$ anneal shifts the GBs from being dark to bright relative to the GIs in as-deposited and annealed samples, respectively. The relatively dark signal at GBs before the $CdCl_2$ becomes brighter after the $CdCl_2$ treatment, suggesting that the GBs become more efficient current collectors than GIs. These results clearly show that the $CdCl_2$ treatment can significantly alter carrier-transport properties. Additional spatially correlated measurements are needed to enhance the understanding of the transport and recombination.

The TI technique can directly map the local spatial variations in charge-carrier transport, with the capability of probing at any localized area, including individual GIs and GBs. Figure 2 shows a schematic. A highly focused e-beam is fixed at a point or scanned in a line (line scan mode) to generate excess carriers within a micro- to nanosized volume of subsurface material. An optical fiber with an aperture diameter of 300 nm acts as a near-field scanning optical microscope (NSOM) probe to scan the sample surface for light collection. The luminescence from the sample is collected in the near field, allowing the possibility of higher spatial resolution than the diffraction limit.[43,44] Also, the setup can be used for NFCL imaging, which can yield similar results as conventional CL.[40,41] This NFCL makes the TI technique more versatile and more convenient to probe the area of interest.

A

B
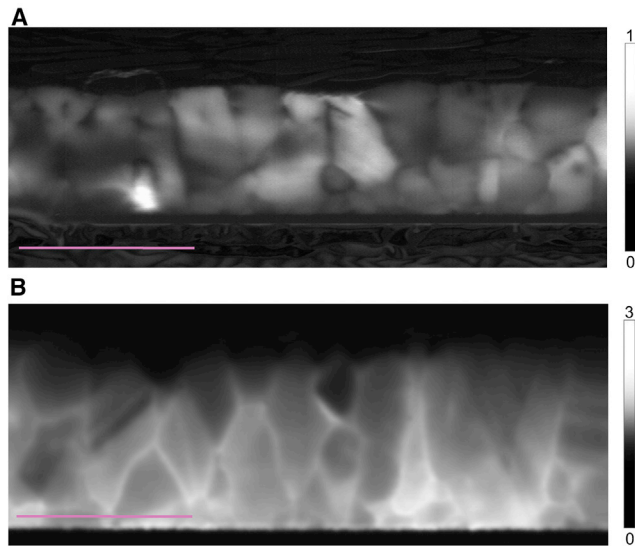
Figure 1. Cross-sectional EBIC Results

(A) Cell with as-deposited CdTe showing dark contrast on the GBs, in a linear scale ranging from 0 (black) to 1 (white).

(B) A $CdCl_2$-treated cell showing high current at the GBs, in a linear scale ranging from 0 (black) to 3 (white). Scale bar: 6 μm.

As-Deposited CdTe

The CdTe film exhibits low quality before the $CdCl_2$ anneal (Figure 3). Similar to CL analysis,[19] apparent boundaries in the NFCL image (Figure 3A) are caused by large inhomogeneous distributions of defects inside grains. Figure 3C shows electron backscatter diffraction (EBSD) measurements on the same location, based on the marks made by a focused ion beam (FIB). The EBSD mapping could not be correlated well with the NFCL image, indicating the poor quality of the intragrain material. Similarly, KPFM does not correlate well with the EBSD (Figure 3B), indicating relatively small variations in the surface potential that are not correlated with GBs.

In the TI measurement, the e-beam rasters on a line a few orders of magnitude faster than the TI scan (8 ms per point) and the carrier generation can be treated as a steady-state line excitation. This line excitation is shown at the top of Figure 3D. TI measures a distribution of luminescence from the carrier recombination, which can be seen to be steadily decreasing away from the excitation line. The net carrier transport is in the direction perpendicular to the carrier generation line. In this case, we did not observe a carrier-transport behavior affected noticeably by GBs. This scenario can be described by a simpler diffusion equation than in spot excitation.[45] To analyze an effective diffusion length or transport length, L_{eff}, we model the source as a delta function and use Green's function to solve a diffusion equation with boundary conditions imposed by a free surface of a three-dimensional half-space; L_{eff} is extracted via a nonlinear least-squares fit.[46] The distance from left to right in Figure 3D ranges from 0 to 6 μm; the decay is from the top of the image (e-beam excitation position) to the bottom, where almost no measurable radiative recombination remains. The values of L_{eff} were fitted on every pixel of the TI images along the carrier-transport decay direction. We aligned the fitted lengths with TI mapping in Figure 3D. L_{eff} of the as-deposited sample is ~0.9 μm, and it is relatively uniform throughout the sample.

Carrier Transport in CdTe after the $CdCl_2$ Anneal

After the $CdCl_2$ anneal, the material is less defective. We focus our efforts on resolving the spatial distribution of localized carrier transport around GBs, where
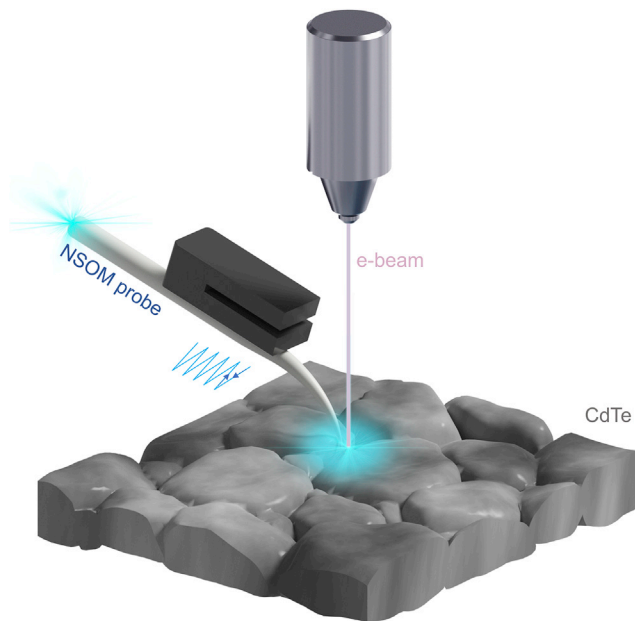
Figure 2. Schematic of TI Experiment

Depending on the kind of analysis, the e-beam may be stationary (as shown above) or scanned on a straight line. The NSOM probe scans on the sample surface to map the localized luminescence generated by the e-beam. The panchromatic light signal is collected via a fiberoptic connection to a Si detector. In the NFCL experiment, the e-beam and NSOM probe are fixed at ∼0.8 µm from each other and the sample is scanned. The optical collection area is limited to the NSOM probe aperture size.

EBIC and KPFM show an electric field. To investigate the effect of GBs on the carrier transport in different directions, the TI measurements were performed on a linear path either perpendicular or parallel to GBs.

Measurements were taken across >10 GBs on 2 different samples. A representative subset of TI measurements for carrier transport parallel to a GB are shown in Figure 4, and additional data are shown in the Supplemental Information, together with EBSD, NFCL, and KPFM measurements. NFCL showed a 4-times higher intensity than the as-deposited sample and clear GI and GB contrast (Figure 4B), which correlates well with the EBSD map (Figure 4A). As indicated in Figure 4B, TI scans were performed to investigate the nonuniform carrier-transport properties in GIs and GBs, with the e-beam line generation approximately perpendicular to the GBs; three TI mappings and the corresponding fitting results are presented in Figures 4D–4F.

Consistent with the EBIC results, KPFM surface-potential mapping shows higher potential at GBs than on GIs (Figure 4C) after the $CdCl_2$ treatment. GBs 1–3 are representative and have ∼41, 62, and 67 mV higher potential than the neighboring GIs (Figure 4H), respectively. Although this is a surface potential rather than a bulk-potential measurement, it indicates that electrostatic fields form at GBs during the $CdCl_2$ treatment. The other GBs in this sample (Figure S1) show similar magnitudes and characteristics.

The TI images have lower light intensity at these GBs around the e-beam excitation line. This is because GBs contain dislocation cores and a higher concentration of defective bonds, so the nonradiative material lifetime is reduced. However, the initially low intensity does not necessarily indicate shorter transport length. Although
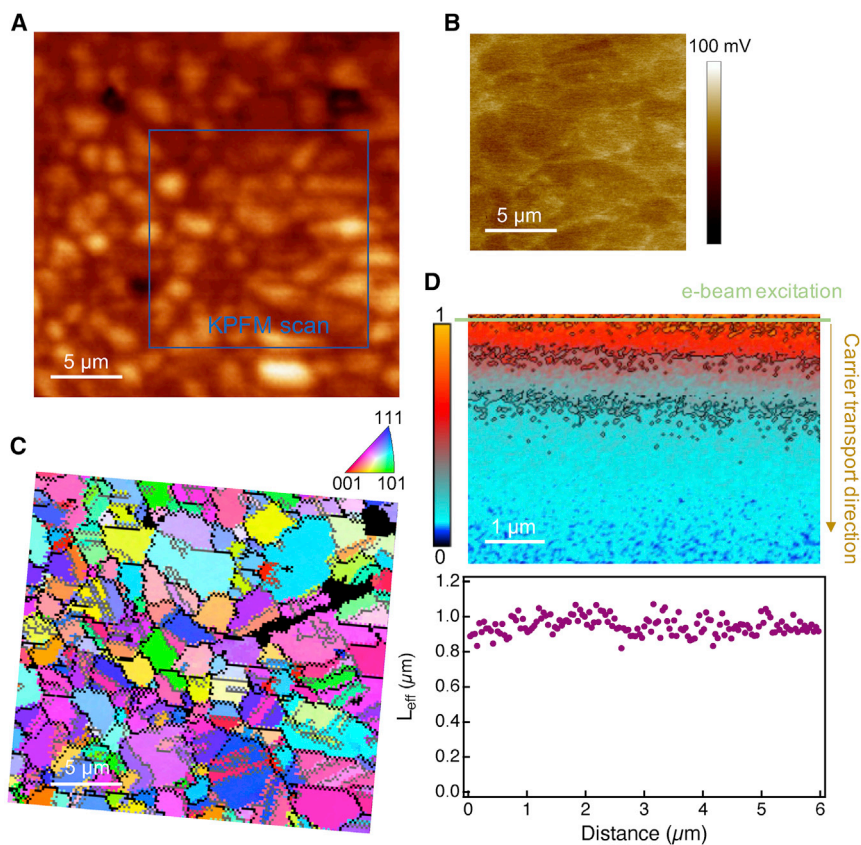
**Figure 3. Results of an As-Deposited CdTe Sample**

(A) NF-CL mapping.

(B) KPFM mapping on the same location.

(C) EBSD mapping.

(D) E-beam excitation (green line) and the luminescence intensity in linear scale from 0 (blue) to 1 (orange) of a random region (top) and (bottom) the corresponding fitting.

GB potentials introduce non-diffusion mechanisms, we evaluate a transport length using the previously described three-dimensional fitting method and align these with the TI maps; the transport lengths were found to be higher at GBs. For example, in Figure 4D, the GI has a transport length of 1.9 μm, whereas GB1 has an enhanced transport length of ~3.0 μm. The transport-length enhancement is defined as

$$\frac{L_{eff\ GB} - L_{eff\ GI}}{L_{eff\ GI}} \times 100\%. \qquad \text{(Equation 1)}$$

The transport-length enhancement of GB1 is ~58%. GB2 has a length that is 69% enhancement relative to the neighboring GIs (Figure 4E), whereas GB3 showed a slightly longer transport length (9% enhancement) compared to the GIs (Figure 4F). Although the GB has a lower light intensity near the excitation region, the collected light intensity decays more slowly, which yields an enhanced L_{eff}. We show line profiles from a GI and a GB in Figure 4G as an example. Figure 4H shows that stronger GB surface potential correlates to more enhancement. More results from different GBs are included in Table 1 to view the relationship between the enhanced transport length and the electrostatic potential, and additional detailed TI results are shown in Figures S1 and S2. The KPFM profile is averaged along the GB, and the technique has a resolution of ~10 mV. Measurement uncertainty is also included by taking the average value and standard deviation of data points around the GB region; additional details are shown in Experimental Procedures. Figure 4I
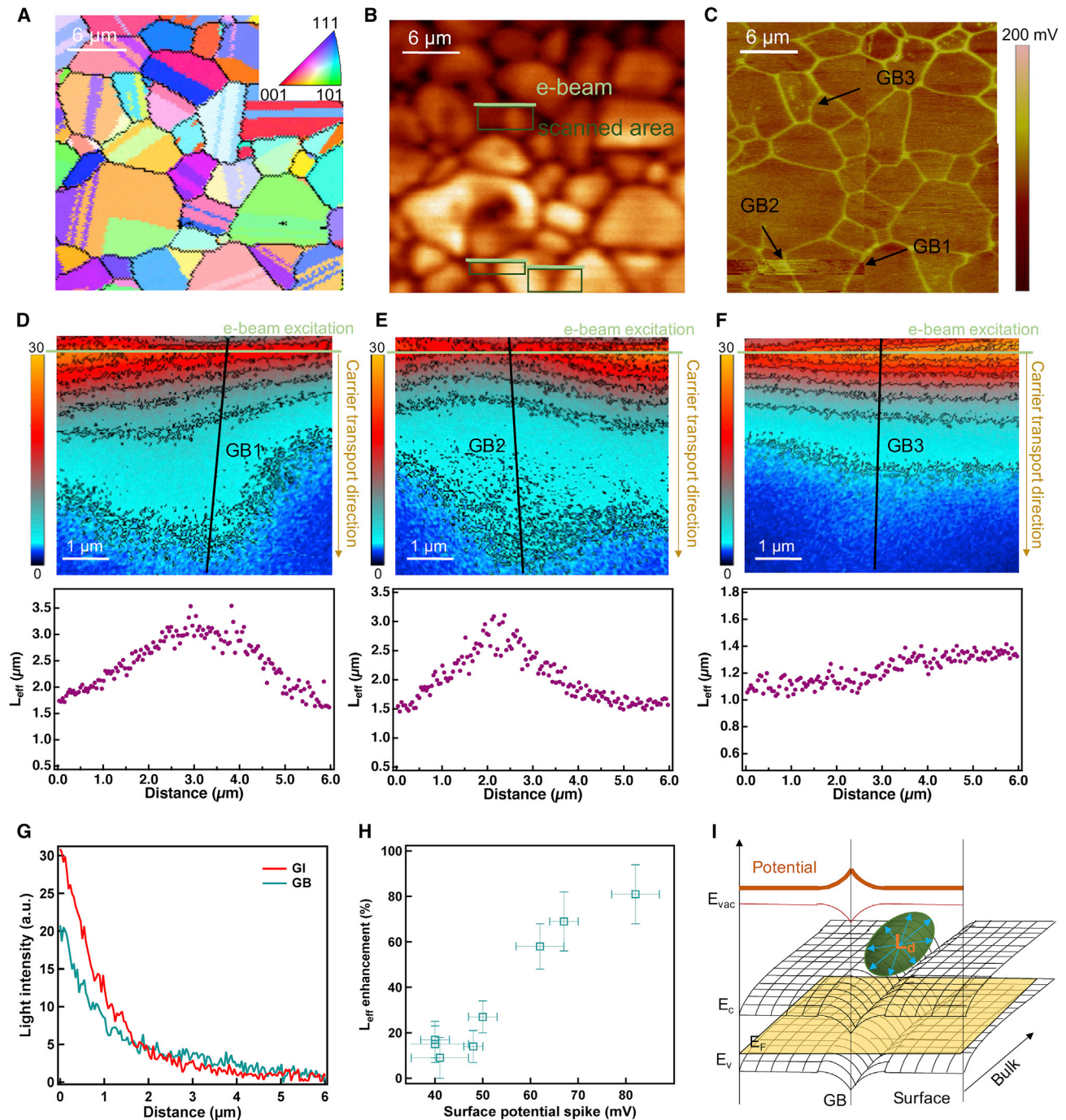
Figure 4. Results of CdCl$_2$-Treated Sample

(A) EBSD, (B) NFCL, (C) KPFM mapping on the same location. Four of ~15 × 15 µm² KPFM images were stitched together to ensure high resolution scans on the same location with EBSD and NFCL.

(D–F) Top: carrier-transport mapping indicating the luminescence intensity on a linear scale ranging from 0 (blue) to 30 (orange) for the GB1, GB2, and GB3 regions. The green line shows the position of the e-beam excitation and the black line shows the GB location. Bottom: the corresponding transport lengths obtained by fitting each of the 256 vertical lines of the TI images above, from left to right.

(G) Example of 2 line profiles extracted from GB1 (D), 1 on GI and 1 close to the GB.

(H) The relationship between the GB surface-potential contrast and transport-length enhancement for 8 GBs on the same sample. Error bars showed the measurement uncertainty by taking the standard deviation of data points around GB.

(I) Schematic of the band structure, surface potential, and transport vector.

Table 1. Surface Potential and TI Results ~8 GBs

GB	Potential Spike (mV)	L_{eff} at GI (μm)	L_{eff} at GB (μm)	L_{eff} Enhancement (%)
1	62 ± 5	1.9	3.0 ± 0.2	58 ± 10
2	67 ± 3	1.6	2.7 ± 0.2	69 ± 13
3	41 ± 6	1.1	1.2 ± 0.1	9 ± 9
4	40 ± 3	1.2	1.4 ± 0.1	17 ± 8
5	82 ± 5	1.6	2.9 ± 0.2	81 ± 13
6	40 ± 7	1.3	1.5 ± 0.1	15 ± 8
7	48 ± 2	1.4	1.6 ± 0.1	14 ± 7
8	50 ± 3	1.5	1.9 ± 0.1	27 ± 7

GB, grain boundary; GI, grain interior; TI, transport imaging.

is a schematic indicating that the transport length is not a single value, but rather a vector enhanced in the direction parallel to the charged GB. In general, the higher GB potential leads to downward band bending that attracts electrons (minority carriers) toward the GB and repels holes away from it.

In these TI measurements, the e-beam is estimated to generate $\sim 10^{15}$ cm^{-3} carriers at the excitation core, while the equilibrium hole density is ~ 1–3×10^{14} cm^{-3}. Consequently, at the generation site, the GB potential is screened.[47,48] As the distance from the generation source increases, excess carriers and the screening subsides and the GB potential progressively increases. The GB potential more strongly attracts electrons with increasing distance from the generation source. The steady-state electron distribution is determined by diffusion away from the source as well as by drift toward and along the electrostatic potential extending from the GB. When the electron density is less than the equilibrium hole density, the luminescence is proportional to the electron density. The TI measurement does not have the spatial resolution to reveal the defective GB core. The enhanced transport length shown in TI manifests the pull of the GB potential on electrons as they drift and diffuse away from the generation source. This is manifested by the clear correlation shown in Figure 4H between the GB potential measured by KPFM and the enhanced transport length. TI does not measure diffusion alone but instead transport affected by different variables, including generation characteristics, diffusion, drift, and GB potential.

Consequently, when the e-beam injection forces carrier diffusion in a direction that is perpendicular to the GB, the transport and resulting TI measurements indicate distinct trends. To examine this effect, the e-beam line source was placed parallel to a GB and at different distances from the GB. Figure 5A shows the NFCL image, indicating the distribution of GBs and GIs. When the carrier-generation location is relatively far from the GB, the carrier transport is naturally not affected by GBs, and the TI decay is relatively uniform (Figure 5B). When the carrier source is close to a GB, the transport length is reduced. In this case, the generation is far from the GB, so the downward band bending that attracts electrons is not screened. Furthermore, the line generation causes carrier diffusion toward the GB. The GB potential acts as a sink for electrons and a barrier for electron transport across the GB, enhancing recombination in this region. These effects lead to faster TI decay and weaker luminescence. The e-beam line source is not exactly parallel to the GB, so when the carrier generation is closer to the GB, the light intensity decreases more quickly, as seen in the TI signal contour (Figure 5C).

The TI, CL, KPFM, and EBIC measurements illustrate that GBs can act both as current pathways and recombination centers. In fact, most GBs should illustrate this
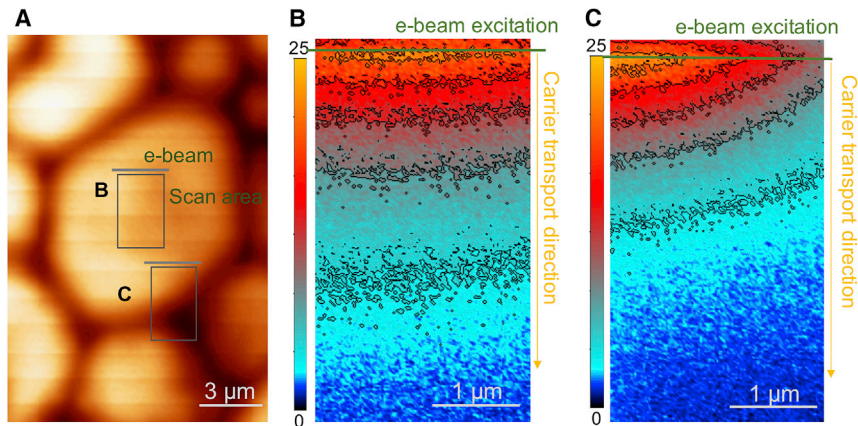
Figure 5. Results of CdCl$_2$-Treated CdTe Sample, with E-Beam Excitation Parallel to GB in TI Scans
(A) NFCL and boxes marking e-beam excitation and scanning regions shown in (B) and (C).
(B) Carrier-transport mapping with carrier generation relatively far away from the targeted GB.
(C) Carrier-transport mapping with carrier generation near a GB. The luminescence intensity is plotted on a linear scale ranging from 0 (blue) to 25 (orange).

behavior. Misoriented GBs are generally defective. NFCL data in Figure 4B and other far-field CL investigations in the literature indicate dark GBs. Here, and in general, CL measurements are done in high injection screening the GB potential and enhancing sensitive to recombination relative to carrier density or drift.[20,49–51] Defective regions will generally have states deeper in the band gap than the Fermi level, pulling bands downward. It is therefore expected that the GB defects form potentials that attract minority carriers, as evidenced by KPFM measurements. The GB potential is typically <100 mV, which is insufficient to claim that the GBs are like interdigitated n-type layers, and instead are better conceptualized as a region slightly less p-type than the grain interior. The accumulation of minority carriers enhances the EBIC signal near the GB more than poor material lifetime near the GB decreases it. Consequently, it is not unphysical for regions near GBs to have enhanced EBIC signals, particularly when carriers can transport adjacent to (rather than within) the GB. Naturally, other effects such as surface recombination may affect the steady-state charge transport.[52] The TI measurements provide a method to image how multiple physical mechanisms affect aggregate transport and recombination.

These results indicate that carrier drift, diffusion, and recombination vary as a function of GB potential, inhomogeneous lifetime, injection orientation, and transport direction. While at first it may be exciting to see enhanced EBIC signals along GBs, the source of the GB potential can be defects. Furthermore, during solar cell operation, the voltage bias will be held near the maximum power point, and electrons will be driven from the transparent conducting oxide layers into the CdTe absorber region, preferentially along the GBs due to their localized potential.[38] This will increase forward current, which, in turn, will lower V_{oc}.[38,53,54] Consequently, the overall effect on performance will be a balance between the additional photocurrent and the reduced voltage caused by the GBs.[38,54] The TI results illustrate how the diffusion length can vary based on position to help quantify potential effects. Here, TI indicates that the diffusion length after CdCl$_2$ treatment is substantively longer than the average absorption depth (several hundred nanometers) of above-band gap photons; thus, additional current collection may fail to compensate for V_{oc} losses. In general, TI in conjunction with KPFM, CL, and EBIC can help assess complex transport and recombination, and it can facilitate engineering these effects in

concert with processes such as group V doping, Cl passivation, deposition or anneals to affect stoichiometry, and back-contact diffusion.

$CdCl_2$ treatment improves CdTe material quality. However, CL indicates that GBs are still defective, and KPFM indicates the formation of minority-carrier attractive potentials around GBs that are sufficient to enhance EBIC signals, but insufficient to claim truly *n*-type GB regions. TI demonstrates that carrier transport varies in distance and direction as a function of electron-hole generation position, GB potential, inhomogeneous recombination, and other material properties. These results provide a new understanding of the complex and aggregate effects of $CdCl_2$ treatment and GB potentials on recombination and transport in polycrystalline CdTe materials. From a broader perspective, the TI technique, coupled with other spatially correlated microscopies, offers a unique capability to map and quantify carrier transport in highly inhomogeneous polycrystalline material systems. This capability can both advance understanding and provide a platform to engineer complex transport to improve performance and further reduce the levelized cost of electricity of polycrystalline solar technology below the cost of fossil fuels.

EXPERIMENTAL PROCEDURES

Resource Availability

Lead Contact
Dr. Chuanxiao Xiao: chuanxiao.xiao@nrel.gov.

Materials Availability
This study did not generate new unique reagents.

Data and Code Availability
All of the data are included in the article and the Supplemental Information. Raw data files are available on request.

Samples

The polycrystalline CdTe thin films were deposited on SnO_2:F-coated soda-lime-glass substrates after MgZnO window-layer deposition. The CdTe films were grown by close-spaced sublimation (CSS) with a substrate temperature of 600°C. The $CdCl_2$ treatment was done in a CSS chamber with O_2 ambient, by vapor $CdCl_2$ at 490°C for 10 min.[55,56]

We made marks by FIB to guide multiple characterization techniques working on the same location. The FIB marks were made by a Ga^+ gun (xT Nova NanoLab 200 FIB/SEM) under a 5-kV beam condition. The FIB marks have an area of ~2 × 2 μm^2 and an ~1-μm depth.

The samples were ion milled by a JEOL cross polisher (IB-09101CP) at a 5° glancing angle to remove surface roughness and FIB damage. The polishing condition was 4 kV for 30 min at room temperature. Then, the samples were further ion milled lightly at 3 kV for 15 min, followed by a 250°C anneal for 5 min to passivate possible surface damage by the previous polishing steps.[57]

TI and NFCL Techniques

The TI and NFCL techniques were performed on an NSOM system (Nanonics Multiview 2000) with a field-emission Nova 630 scanning electron microscope (FE-SEM). The FE-SEM provides a highly focused e-beam fixed at a point or in a line scan mode to generate excess carriers within a micro- to nanosized volume of subsurface material. The NSOM

system used an optical fiber with an aperture diameter of 300 nm as a probe, which also acts as an atomic force microscopy (AFM) probe to scan the sample surface and collect the sample luminescence in the near field. This combination provides high spatial resolution imaging of charge-carrier transport and direct mapping of nonuniform transport properties in polycrystalline thin-film samples. A Si detector collected the panchromatic light emitted from the sample. Two 800-nm long-wavelength pass filters were applied to selectively transmit luminescence to the optical fiber.

In TI scans, the e-beam was scanned in line mode or fixed at a point for carrier generation, and the NSOM probe collected the light emitted from the sample to create luminescence, carrier diffusion, and recombination profiles. In NFCL, the e-beam and the NSOM probe were both fixed at ~0.8 μm in relation to each other while the sample was scanned. The NFCL measurement is similar to conventional CL.[58] However, in conventional CL, the e-beam rasters on every point, and a parabolic mirror collects the emitted light from the sample, including both the point generation and luminescence resulting from carrier diffusion. In NFCL, the sample moves, whereas the excitation and collection points are fixed, thus generating a luminescence map similar to the conventional CL. The collection area on every pixel is limited to the size of the NSOM aperture, thereby limiting the diffusion effects on the resolution. Both TI and NFCL scans were performed at 20-kV, 1.5-nA e-beam conditions at room temperature. The e-beam conditions were the same for TI and NFCL. However, in TI scans, most of the signal was acquired from the carrier-generation source; in contrast, in NFCL, the signal was acquired near the e-beam generation point. The TI and NFCL mapping areas are 256 × 256 pixels, with a dwell time of 8 ms on each point. The TI setup uses NSOM to collect light. It collects only illumination away from the e-beam because the probe shades an area at least larger than its aperture size, when the probe is directly beneath the e-beam. Therefore, the TI results do not have significant contribution from the transition radiation at the sample-vacuum interface.[59,60]

EBIC and EBSD
EBIC was performed using the Nova 630 SEM equipped with a Matelect current amplifier, operating at 3-kV/0.9-nA beam conditions. EBSD measurements were performed on the same FE-SEM using an EDAX Hikari camera, under 20-kV/1.5-nA e-beam conditions. The samples were tilted at 70° to increase the yield of diffracted electrons.

KPFM
KPFM was measured by a Veeco D3100 AFM equipped with the Nanoscope V controller. The measurements were in tapping mode, with a Pt-Ir-coated Si cantilever probe (Nanosensor PPP-EFM). KPFM measures the contact-potential difference between the probe and sample by probing and nullifying the Coulomb force between the probe and the sample. KPFM mapping provides a ~30-nm spatial resolution and a ~10-mV electrical resolution.[61] The KPFM image in Figure 4C was stitched together from several scans.

Combining Multiple Techniques
The FIB marks are 2 × 2 μm² and provide rough guidance for different techniques to study the same location in a region that is ~30 × 30 μm². After collecting the data, the NFCL, EBSD, and KPFM images are manually aligned by close inspection to resolve minor positional shifts. Extraordinarily accurate alignment for these images are not critical, as the grain shapes and boundaries aid correlating results from different techniques (Figure S3). The KPFM spatial resolution is ~30 nm, the NFCL resolution is within 50 nm, and the EBSD resolution is ~20 nm.

The NFCL and TI are acquired on the same setup. In NFCL, the sample is scanned with the e-beam and NSOM probe fixed. In TI, the NSOM probe is moved across the sample, while the e-beam generation and samples are fixed. The resolution in Figures 4 and 5 reflects the accuracy of the NFCL and TI techniques, which are estimated to be within 50 nm.

In Figure 4H and Table 1, the measurement uncertainty is reported using the mean value and the standard deviation. Data points within a 1-μm range (e.g., along the "distance" axis in Figure 4D, bottom panel) of a GB contributes to the measurement uncertainty of the reported L_{eff} values at GB in Table 1, and therefore the L_{eff} enhancement in percentage with respect to GI. The Y error in Figure 4H is attributed to the L_{eff} enhancement uncertainty. The reported potential spike measured using the KPFM is given by the mean value among the spikes measured along the GB; the X error in Figure 4H is ascribed to the standard deviation of the measured potential spikes.

AUTHOR CONTRIBUTIONS
Conceptualization, C.X., N.M.H., and H.M.; Methodology, C.X. and N.M.H.; Software, K.B.; Validation, C.X., C.-S.J., W.K.M., N.M.H., and H.M.; Formal Analysis, C.X., C.-S.J., W.K.M., N.M.H., and H.M.; Investigation, C.X., C.-S.J., N.M.H., and H.M.; Resources, C.X., C.-S.J., M.A., E.C., and H.M.; Data Curation, C.X., C.-S.J., W.K.M., N.M.H., and H.M.; Writing—Original Draft, C.X.; Writing—Review and Editing, all authors; Visualization, C.X.; Supervision, C.X., W.K.M., M.M.A., N.H.M., and H.M.; Project Administration, C.X., M.M.A., N.H.M., and H.M.; Funding Acquisition, H.M.

DECLARATION OF INTERESTS
The authors declare no competing interests.

REFERENCES

1. Green, M.A., Dunlop, E.D., Levi, D.H., Hohl-Ebinger, J., Yoshita, M., and Ho-Baillie, A.W.Y. (2019). Solar cell efficiency tables (version 54). Prog. Photovolt. Res. Appl. 27, 565–575.

2. National Renewable Energy Laboratory. Best Research-Cell Efficiency Chart, Photovoltaic Research. https://www.nrel.gov/pv/cell-efficiency.html.

3. Gloeckler, M., Sankin, I., and Zhao, Z. (2013). CdTe solar cells at the threshold to 20% efficiency. IEEE J. Photovolt. 3, 1389–1393.

4. Kephart, J.M., McCamy, J.W., Ma, Z., Ganjoo, A., Alamgir, F.M., and Sampath, W.S. (2016). Band alignment of front contact layers for high-efficiency CdTe solar cells. Sol. Energy Mater. Sol. Cells 157, 266–275.

5. Paudel, N.R., and Yan, Y. (2014). Enhancing the photo-currents of CdTe thin-film solar cells in both short and long wavelength regions. Appl. Phys. Lett. 105, 183510.

6. Poplawsky, J.D., Guo, W., Paudel, N., Ng, A., More, K., Leonard, D., and Yan, Y. (2016). Structural and compositional dependence of the CdTe$_x$Se$_{1-x}$ alloy layer photoactivity in CdTe-based solar cells. Nat. Commun. 7, 12537.

7. Fiducia, T.A.M., Mendis, B.G., Li, K., Grovenor, C.R.M., Munshi, A.H., Barth, K., Sampath, W.S., Wright, L.D., Abbas, A., Bowers, J.W., et al. (2019). Understanding the role of selenium in defect passivation for highly efficient selenium-alloyed cadmium telluride solar cells. Nat. Energy 4, 504–511.

8. Burst, J.M., Duenow, J.N., Albin, D.S., Colegrove, E., Reese, M.O., Aguiar, J.A., Jiang, C.-S., Patel, M.K., Al-Jassim, M.M., Kuciauskas, D., et al. (2016). CdTe solar cells with open-circuit voltage breaking the 1 V barrier. Nat. Energy 1, 1–8.

9. Metzger, W.K., Grover, S., Lu, D., Colegrove, E., Moseley, J., Perkins, C.L., Li, X., Mallick, R., Zhang, W., Malik, R., et al. (2019). Exceeding 20% efficiency with in situ group V doping in polycrystalline CdTe solar cells. Nat. Energy 4, 837–845.

10. Ma, J., Kuciauskas, D., Albin, D., Bhattacharya, R., Reese, M., Barnes, T., Li, J.V., Gessert, T., and Wei, S.-H. (2013). Dependence of the minority-carrier lifetime on the stoichiometry of CdTe using time-resolved photoluminescence and first-principles calculations. Phys. Rev. Lett. 111, 067402.

11. Albin, D.S., Kuciauskas, D., Ma, J., Metzger, W.K., Burst, J.M., Moutinho, H.R., and Dippo, P.C. (2014). Cd-rich and Te-rich low-temperature photoluminescence in cadmium telluride. Appl. Phys. Lett. 104, 092109.

12. Li, J., Diercks, D.R., Ohno, T.R., Warren, C.W., Lonergan, M.C., Beach, J.D., and Wolden, C.A. (2015). Controlled activation of ZnTe:Cu contacted CdTe solar cells using rapid thermal processing. Sol. Energy Mater. Sol. Cells 133, 208–215.

13. Uličná, S., Isherwood, P.J.M., Kaminski, P.M., Walls, J.M., Li, J., and Wolden, C.A. (2017). Development of ZnTe as a back contact material for thin film cadmium telluride solar cells. Vacuum 139, 159–163.

14. McCandless, B.E., Moulton, L.V., and Birkmire, R.W. (1997). Recrystallization and sulfur diffusion in CdCl$_2$-treated CdTe/CdS thin films. Prog. Photovolt. Res. Appl. 5, 249–260.

15. Metzger, W.K., Albin, D., Romero, M.J., Dippo, P., and Young, M. (2006). CdCl$_2$ treatment, S diffusion, and recombination in polycrystalline CdTe. J. Appl. Phys. 99, 103703.

16. Terheggen, M., Heinrich, H., Kostorz, G., Romeo, A., Baetzner, D., Tiwari, A.N., Bosio, A., and Romeo, N. (2003). Structural and chemical interface characterization of CdTe solar cells by transmission electron microscopy. Thin Solid Films 431–432, 262–266.

17. Komin, V., Tetali, B., Viswanathan, V., Yu, S., Morel, D.L., and Ferekides, C.S. (2003). The effect of the CdCl$_2$ treatment on CdTe/CdS thin film solar cells studied using deep level transient spectroscopy. Thin Solid Films 431–432, 143–147.

18. Zhang, L., Da Silva, J.L.F., Li, J., Yan, Y., Gessert, T.A., and Wei, S.-H. (2008). Effect of copassivation of Cl and Cu on CdTe grain boundaries. Phys. Rev. Lett. 101, 155501.

19. Moseley, J., Metzger, W.K., Moutinho, H.R., Paudel, N., Guthrey, H.L., Yan, Y., Ahrenkiel, R.K., and Al-Jassim, M.M. (2015). Recombination by grain-boundary type in CdTe. J. Appl. Phys. 118, 025702.

20. Moseley, J., Rale, P., Collin, S., Colegrove, E., Guthrey, H., Kuciauskas, D., Moutinho, H., Al-Jassim, M., and Metzger, W.K. (2018). Luminescence methodology to determine grain-boundary, grain-interior, and surface recombination in thin-film solar cells. J. Appl. Phys. 124, 113104.

21. Harvey, S.P., Teeter, G., Moutinho, H., and Al-Jassim, M.M. (2015). Direct evidence of enhanced chlorine segregation at grain boundaries in polycrystalline CdTe thin films via three-dimensional TOF-SIMS imaging. Prog. Photovolt. Res. Appl. 23, 838–846.

22. Mao, D., Blatz, G., Wickersham, C.E., and Gloeckler, M. (2016). Correlative impurity distribution analysis in cadmium telluride (CdTe) thin-film solar cells by ToF-SIMS 2D imaging. Sol. Energy Mater. Sol. Cells 157, 65–73.

23. Tuteja, M., Koirala, P., MacLaren, S., Collins, R., and Rockett, A. (2015). Direct observation of electrical properties of grain boundaries in sputter-deposited CdTe using scan-probe microwave reflectivity based capacitance measurements. Appl. Phys. Lett. 107, 142106.

24. Tuteja, M., Koirala, P., Palekis, V., MacLaren, S., Ferekides, C.S., Collins, R.W., and Rockett, A.A. (2016). Direct observation of CdCl$_2$ treatment induced grain boundary carrier depletion in CdTe solar cells using scanning probe microwave reflectivity based capacitance measurements. J. Phys. Chem. C 120, 7020–7024.

25. Taylor, A.A., Major, J.D., Kartopu, G., Lamb, D., Duenow, J., Dhere, R.G., Maeder, X., Irvine, S.J.C., Durose, K., and Mendis, B.G. (2015). A comparative study of microstructural stability and sulphur diffusion in CdS/CdTe photovoltaic devices. Sol. Energy Mater. Sol. Cells 141, 341–349.

26. Poplawsky, J.D., Li, C., Paudel, N.R., Guo, W., Yan, Y., and Pennycook, S.J. (2016). Nanoscale doping profiles within CdTe grain boundaries and at the CdS/CdTe interface revealed by atom probe tomography and STEM EBIC. Sol. Energy Mater. Sol. Cells 150, 95–101.

27. Yang, J.-H., Yin, W.-J., Park, J.-S., Metzger, W., and Wei, S.-H. (2016). First-principles study of roles of Cu and Cl in polycrystalline CdTe. J. Appl. Phys. 119, 045104.

28. Orellana, W., Menéndez-Proupin, E., and Flores, M.A. (2019). Self-compensation in chlorine-doped CdTe. Sci. Rep. 9, 9194.

29. Jiang, C.S., Moutinho, H.R., Moseley, J., Kanevce, A., Duenow, J.N., Colegrove, E., Xiao, C., Metzger, W.K., and Al-Jassim, M.M. (2017). Simultaneous examination of grain-boundary potential, recombination, and photocurrent in CdTe solar cells using diverse nanometer-scale imaging. https://ieeexplore.ieee.org/document/8366391.

30. Poplawsky, J.D., Paudel, N.R., Li, C., Parish, C.M., Leonard, D., Yan, Y., and Pennycook, S.J. (2014). Direct imaging of Cl- and Cu-induced short-circuit efficiency changes in CdTe solar cells. Adv. Energy Mater. 4, 1400454.

31. Yan, Y., Yin, W.-J., Wu, Y., Shi, T., Paudel, N.R., Li, C., Poplawsky, J., Wang, Z., Moseley, J., Guthrey, H., et al. (2015). Physics of grain boundaries in polycrystalline photovoltaic semiconductors. J. Appl. Phys. 117, 112807.

32. Li, C., Wu, Y., Poplawsky, J., Pennycook, T.J., Paudel, N., Yin, W., Haigh, S.J., Oxley, M.P., Lupini, A.R., Al-Jassim, M., et al. (2014). Grain-boundary-enhanced carrier collection in CdTe solar cells. Phys. Rev. Lett. 112, 156103.

33. Visoly-Fisher, I., Cohen, S.R., Ruzin, A., and Cahen, D. (2004). How polycrystalline devices can outperform single-crystal ones: thin film CdTe/CdS solar cells. Adv. Mater. 16, 879–883.

34. Visoly-Fisher, I., Cohen, S.R., Gartsman, K., Ruzin, A., and Cahen, D. (2006). Understanding the beneficial role of grain boundaries in polycrystalline solar cells from single-grain-boundary scanning probe microscopy. Adv. Funct. Mater. 16, 649–660.

35. Duenow, J.N., Burst, J.M., Albin, D.S., Kuciauskas, D., Johnston, S.W., Reedy, R.C., and Metzger, W.K. (2014). Single-crystal CdTe solar cells with Voc greater than 900 mV. Appl. Phys. Lett. 105, 053903.

36. Burst, J.M., Duenow, J.N., Kanevce, A., Moutinho, H.R., Jiang, C.S., Al-Jassim, M.M., Reese, M.O., Albin, D.S., Aguiar, J.A., Colegrove, E., et al. (2016). interface characterization of single-crystal CdTe solar cells with Voc > 950 mV. IEEE J. Photovolt. 6, 1650–1653.

37. Zhao, Y., Boccard, M., Liu, S., Becker, J., Zhao, X.-H., Campbell, C.M., Suarez, E., Lassise, M.B., Holman, Z., and Zhang, Y.-H. (2016). Monocrystalline CdTe solar cells with open-

circuit voltage over 1 V and efficiency of 17%. Nat. Energy *1*, 1–7.

38. Metzger, W.K., and Gloeckler, M. (2005). The impact of charged grain boundaries on thin-film solar cells and characterization. J. Appl. Phys. *98*, 063701.

39. Jin, Y., and Dunham, S.T. (2017). The impact of charged grain boundaries on CdTe solar cell: EBIC measurements not predictive of device performance. IEEE J. Photovolt. *7*, 329–334.

40. Xiao, C., Jiang, C.-S., Moseley, J., Simon, J., Schulte, K., Ptak, A.J., Johnston, S., Gorman, B., Al-Jassim, M., Haegel, N.M., et al. (2017). Near-field transport imaging applied to photovoltaic materials. Sol. Energy *153*, 134–141.

41. Xiao, C., Jiang, C.-S., Liu, J., Norman, A., Moseley, J., Schulte, K., Ptak, A.J., Gorman, B., Al-Jassim, M., Haegel, N.M., and Moutinho, H. (2019). Carrier-transport study of gallium arsenide hillock defects. Microsc. Microanal. *25*, 1160–1166.

42. Edwards, P.R., Galloway, S.A., and Durose, K. (2000). EBIC and luminescence mapping of CdTe/CdS solar cells. Thin Solid Films *372*, 284–291.

43. Dunn, R.C. (1999). Near-field scanning optical microscopy. Chem. Rev. *99*, 2891–2928.

44. Lewis, A., Taha, H., Strinkovski, A., Manevitch, A., Khatchatouriants, A., Dekhter, R., and Ammann, E. (2003). Near-field optics: from subwavelength illumination to nanometric shadowing. Nat. Biotechnol. *21*, 1378–1386.

45. Haegel, N.M. (2013). Integrating electron and near-field optics: dual vision for the nanoworld. Nanophotonics *3*, 75–89.

46. Blaine, K.E., Phillips, D.J., Frenzen, C.L., Scandrett, C., and Haegel, N.M. (2012). Three-dimensional transport imaging for the spatially resolved determination of carrier diffusion length in bulk materials. Rev. Sci. Instrum. *83*, 043702.

47. Metzger, W.K., Ahrenkiel, R.K., Dashdorj, J., and Friedman, D.J. (2005). Analysis of charge separation dynamics in a semiconductor junction. Phys. Rev. B Condens. Matter Mater. Phys. *71*, 035301.

48. Metzger, W.K., Romero, M.J., Dippo, P., and Young, M. (2006). Characterizing recombination in cdte solar cells with time-resolved photoluminescence. https://ieeexplore.ieee.org/document/4059640.

49. Ahrenkiel, R.K. (1993). Minority Carriers in III-V Semiconductors: Physics and Applications (Academic Press).

50. Duenow, J.N., and Metzger, W.K. (2019). Back-surface recombination, electron reflectors, and paths to 28% efficiency for thin-film photovoltaics: a CdTe case study. J. Appl. Phys. *125*, 053101.

51. Yoon, Y., Yang, W.D., Ha, D., Haney, P.M., Hirsch, D., Yoon, H.P., Sharma, R., and Zhitenev, N.B. (2019). Unveiling defect-mediated charge-carrier recombination at the nanometer scale in polycrystalline solar cells. ACS Appl. Mater. Interfaces *11*, 47037–47046.

52. Van Roosbroeck, W. (1955). Injected current carrier transport in a semi-infinite semiconductor and the determination of lifetimes and surface recombination velocities. J. Appl. Phys. *26*, 380–391.

53. Gaury, B., and Haney, P.M. (2016). Charged grain boundaries reduce the open-circuit voltage of polycrystalline solar cells-an analytical description. J. Appl. Phys. *120*, 234503.

54. Gloeckler, M., Sites, J.R., and Metzger, W.K. (2005). Grain-boundary recombination in Cu(In,Ga)Se$_2$ solar cells. J. Appl. Phys. *98*, 113704.

55. Amarasinghe, M., Colegrove, E., Moseley, J., Moutinho, H., Albin, D., Duenow, J., Jensen, S., Kephart, J., Sampath, W., Sivananthan, S., et al.

(2018). Obtaining large columnar CdTe grains and long lifetime on nanocrystalline CdSe, MgZnO, or CdS layers. Adv. Energy Mater. *8*, 1702666.

56. Amarasinghe, M., Colegrove, E., Moutinho, H., Albin, D., Duenow, J., Johnston, S., Kephart, J., Sampath, W., Al-Jassim, M., Sivananthan, S., et al. (2018). Influence of CdTe deposition temperature and window thickness on CdTe grain size and lifetime after CdCl$_2$ recrystallization. IEEE J. Photovolt. *8*, 600–603.

57. Johnston, S., Albin, D., Hacke, P., Harvey, S.P., Moutinho, H., Jiang, C.-S., Xiao, C., Parikh, A., Nardone, M., Al-Jassim, M., et al. (2018). Imaging, microscopic analysis, and modeling of a CdTe module degraded by heat and light. Sol. Energy Mater. Sol. Cells *178*, 46–51.

58. Xiao, C., Li, Z., Guthrey, H., Moseley, J., Yang, Y., Wozny, S., Moutinho, H., To, B., Berry, J.J., Gorman, B., et al. (2015). Mechanisms of electron-beam-induced damage in perovskite thin films revealed by cathodoluminescence spectroscopy. J. Phys. Chem. C *119*, 26904–26911.

59. Mendis, B.G., Howkins, A., Stowe, D., Major, J.D., and Durose, K. (2016). The role of transition radiation in cathodoluminescence imaging and spectroscopy of thin-foils. Ultramicroscopy *167*, 31–42.

60. Kuttge, M., Vesseur, E.J.R., Koenderink, A.F., Lezec, H.J., Atwater, H.A., García de Abajo, F.J., and Polman, A. (2009). Local density of states, spectrum, and far-field interference of surface plasmon polaritons probed by cathodoluminescence. Phys. Rev. B Condens. Matter Mater. Phys. *79*, 113405.

61. Xiao, C., Jiang, C.-S., Harvey, S.P., Sulas, D., Chen, X., Liu, J., Pan, J., Moutinho, H., Norman, A., Hacke, P., et al. (2019). Large-area material and junction damage in c–Si solar cells by potential-induced degradation. Solar RRL *3*, 1800303.